Effect of ZIF-8 Crystal Size on the O2 Electro-Reduction Performance of Pyrolyzed Fe–N–C Catalysts

Vanessa Armel, Julien Hannauer, Frédéric Jaouen

Catalysts **2015**, *5*, 1333-1351; doi:10.3390/catal5031333

OPEN ACCESS

catalysts

ISSN 2073-4344

www.mdpi.com/journal/catalysts

Article

Effect of ZIF-8 Crystal Size on the O_2 Electro-Reduction Performance of Pyrolyzed Fe–N–C Catalysts

Vanessa Armel, Julien Hannauer and Frédéric Jaouen *

Institut Charles Gerhardt Montpellier UMR 5253, CNRS, Université de Montpellier, 34095 Montpellier Cedex 5, France; E-Mails: vanessa.armel@univ-montp2.fr (V.A.); julien.hannauer@univ-montp2.fr (J.H.)

* Author to whom correspondence should be addressed; E-Mail: frederic.jaouen@univ-montp2.fr; Tel.: +33-4-6714-3211; Fax: +33-4-6714-3304.

Academic Editor: Minhua Shao

Received: 26 June 2015 / Accepted: 17 July 2015 / Published: 24 July 2015

Abstract: The effect of ZIF-8 crystal size on the morphology and performance of Fe–N–C catalysts synthesized via the pyrolysis of a ferrous salt, phenanthroline and the metal-organic framework ZIF-8 is investigated in detail. Various ZIF-8 samples with average crystal size ranging from 100 to 1600 nm were prepared. The process parameters allowing a templating effect after argon pyrolysis were investigated. It is shown that the milling speed, used to prepare catalyst precursors, and the heating mode, used for pyrolysis, are critical factors for templating nano-ZIFs into nano-sized Fe–N–C particles with open porosity. Templating could be achieved when combining a reduced milling speed with a ramped heating mode. For templated Fe–N–C materials, the performance and activity improved with decreased ZIF-8 crystal size. With the Fe–N–C catalyst templated from the smallest ZIF-8 crystals, the current densities in H_2/O_2 polymer electrolyte fuel cell at 0.5 V reached *ca.* 900 mA cm^{-2}, compared to only *ca.* 450 mA cm^{-2} with our previous approach. This templating process opens the path to a morphological control of Fe–N–C catalysts derived from metal-organic frameworks which, when combined with the versatility of the coordination chemistry of such materials, offers a platform for the rational design of optimized Metal–N–C catalysts.

Keywords: metal organic framework; electrocatalysis; fuel cell; oxygen reduction; non precious metal; templating

---

1. Introduction

Fuel cells offer a combination of efficiency and power density that meets the requests of the most demanding applications, and, in particular, those of the transportation sector [1,2]. Among the fuel cells allowing fast start-up and shut-down operation, an imperative criterion for the automotive industry, the polymer electrolyte membrane fuel cell (PEMFC) is today the most advanced technology due to the existence of proton conductive polymer membranes [3,4]. While PEMFCs have reached the commercialisation level for materials handling vehicles and, since recently, for personal automobiles that are being released in Japan and California, its long term success is bound to cost and sustainability. These two aspects are intimately linked to the usage of platinum for catalyzing the anodic and cathodic reactions. Ultimately, the accessibility to enough platinum is questionable if the PEMFC technology is to replace internal combustion engines. Since 80%–90% of platinum in a PEMFC is needed to catalyze the sluggish oxygen reduction reaction (ORR) [5], reducing the Pt content at the cathode or replacing Pt-based catalysts by catalysts based on Earth-abundant elements is a topic of intense research since 2003 [6].

Catalysts based on iron, cobalt, nitrogen and carbon that feature Metal–N_xC_y moieties covalently integrated in N-doped carbons have emerged as a promising alternative to Pt-based catalysts [6–12]. Rational approaches for the selection of metal, nitrogen and carbon precursors, for the synthetic conditions and for more durable Metal–N–C catalysts, are, however, still needed. In 2011, the use of metal organic frameworks (MOFs) as sacrificial N and C precursors for the synthesis of Co– and Fe–N–C catalysts was first reported [8,13]. In the approach by Liu's group, the cobalt ions were engaged in the MOF structure and therefore ideally dispersed and coordinated to nitrogen atoms [13]. The inherent disadvantage is the high content of cobalt in Co-based MOFs, 30–40 wt. %. This is well above the optimum content for Me–N–C catalyst precursors before pyrolysis, typically below 2–3 wt. % [7,14–16]. Too large Fe or Co contents lead to the formation of highly graphitized carbon structures during pyrolysis [13,17]. In such graphitized structures, the number of MeN_xC_y active sites is low, which leads to a low ORR activity [18,19]. In order to maximize the activity, it is necessary to reach a high specific area, and especially a high microporous area [7,20–22]. In the approach by Dodelet's group, a Zn-based MOF was combined with Fe(II) and phenanthroline in order to prepare a catalyst precursor which, after pyrolysis in Ar and then NH_3, resulted in a Fe–N–C catalyst with unprecedented initial power performance in PEMFC [8]. The Zn-based MOF used in 2011 by Dodelet's group was ZIF-8, a well-known zeolitic imidazolate framework (ZIF) [23,24], commercially available under the trade name Basolite® Z1200 (produced by BASF, purchased from Sigma Aldrich, St. Louis, MO, USA), referred to hereafter as Basolite®. ZIF-8 has a sodalite topology and is entirely microporous with a BET area of *ca.* 1600 m^2 g^{-1} [23]. Fe–N–C catalysts derived with various approaches from Fe(II) acetate, 1,10-phenanthroline and ZIF-8 but sharing a common pyrolytic step in NH_3, still represent the state-of-the-art in terms of initial power performance in PEMFC [8,10,25–27]. They however suffer from a poor durability, with *ca.* halved power performance after 50 h of operation, characteristic for NH_3-pyrolyzed catalysts [8,10,28]. In contrast, Fe–N–C catalysts derived from Fe(II), 1,10-phenanthroline and ZIF-8 but pyrolyzed in Argon are initially less active but more stable [8,29,30]. Other Fe– and Fe–Co–N–C catalysts pyrolyzed in inert atmosphere have resulted in

a constant current density at 0.4–0.5 V over several hundred hours of operation in PEMFC, a promising achievement toward more durable Me–N–C catalysts [9,31].

Since the first reports on the synthesis of Metal–N–C materials via the sacrificial pyrolysis of microporous ZIFs [8,13], modifications of the preparation of the catalyst precursor from Fe(II) acetate, N-ligands and ZIF-8 have minimized the formation of undesired iron particles during pyrolysis. Low energy milling of the dry precursor powders has been shown to optimise the dispersion of ferrous ions and to favour the formation of FeN_xC_y moieties during pyrolysis [25,32]. The replacement of Fe(II) and 1,10-phenanthroline (phen) by an iron porphyrin was also shown to preferentially result in the formation of FeN_xC_y moieties after pyrolysis [33]. Alternative Zn-based ZIFs have also started being investigated, using a one-pot synthesis approach [10,26]. The impregnation of ZIF-8 with furfuryl alcohol introduced mesoporosity in the resulting Fe–N–C catalysts [34]. However, the increased mesoporous volume did not increase the fuel cell performance.

To a large extent, the transport properties of Metal–N–C cathodes today limit the fuel cell performance at high load [6]. Identifying rational approaches to optimize transport properties without negatively affecting the ORR activity of the most active or most stable Me–N–C catalysts reported to date is therefore important. Hence, controlling the size of ZIF crystals before pyrolysis and controlling all process parameters in order to template nanosized ZIF crystals into nano-sized catalytic Me–N–C particles is a promising approach. It could significantly reduce the average diffusion length for O_2 molecules from the electrode macropores to the active FeN_4 sites located in intra-particle pores. In the commercial ZIF-8, Basolite®, the crystal size ranges from 200 to 500 nm, which is not optimum [8].

Hitherto, the size effect of ZIF crystals on the activity and accessibility of ORR active sites in Me–N–C catalysts derived from the pyrolysis of ZIFs has not been investigated in depth. Recent attempts include Co–N–C catalysts derived from ZIF-67 and metal-free N–C catalysts derived from ZIF-8 [35,36]. ZIF-67, a ZIF comprising Co(II) ion ligated with 2-MeIm organised in sodalite topology, was synthesized in three average sizes of 300, 800 and 1700 nm. ZIF-67 powders were then pyrolyzed in Ar at 600–900 °C to form Co–N–C catalysts. The Co–N–C catalyst derived from ZIF-67 with the smallest crystal size of 300 nm showed a higher activity in rotating disk electrode measurements in 0.1 M $HClO_4$ [35]. SEM and TEM images showed a remarkable templating of the rhombic dodecahedron shape of ZIF-67 nanocrystals into Co–N–C catalytic particles with similar size. The second study reported the synthesis of ZIF-8 crystals with average size of 60 nm [36]. ZIF-8 was pyrolyzed in N_2 at 700–1000 °C. A templating effect was similarly observed, even after pyrolysis at 1000 °C. A high ORR activity of the resulting N-doped carbons was measured in 0.1 M KOH. The effect of smaller catalytic Fe(Co)–N–C particles has however not yet been demonstrated in fuel cell measurements at high current density, where a short diffusion path for O_2 is expected to be most beneficial. The restricted current densities of a few $mA \cdot cm^{-2}$ in rotating disk electrode measurements cannot inform whether such templated catalysts perform better in a fuel cell.

The development of synthetic methods to control the size of MOF or ZIF crystals is relatively recent by itself [37–43]. Of particular interest, the rapid crystallization at room temperature of Zn(II) and 2-MeIm into ZIF-8 in either methanol or aqueous solution is now well established [36,42,44,45]. Control of the size of ZIF-8 crystals has been gained with the approaches of (i) modulating-ligand [38,44] (ii) surfactants [40] and (iii) excess-ligands [37,42,45]. The first approach relies on the competition for Zn(II) ions between 2-MeIm and a second modulating ligand

added in the reagent solution. For example, large ZIF-8 crystals of *ca.* 1 μm were obtained from Zn(II) and 2-MeIm in the presence of the modulating ligand 1-MeIm [44]. In the absence of 1-MeIm, ZIF-8 crystals of 60–70 nm were obtained. In the presence of another modulating ligand, n-butylamine, ultra small ZIF-8 crystals of 9–10 nm could be obtained. The effects were rationalized on the basis of the ability of the modulating ligand to deprotonate 2-MeIm during the nucleation of ZIF-8. The second approach relies on the use of surfactants that stabilize nanosized ZIF-8 crystals [40]. With surfactants, phase pure ZIF-8 crystals of sub-100 nm size could be obtained at nearly stoichiometric ratio 2:1 for 2-MeIm:Zn(II). The third approach relies on overstoichiometric ratios of 2-MeIm:Zn(II) in the reagent solution. The excess of 2-MeIm results in a high density of nucleation sites for the crystallization of ZIF-8, and hence in smaller crystals [37,42,45]. Molar ratios of 2-MeIm to Zn(II) from four to 200 have been investigated resulting in ZIF-8 crystals with size ranging from 1900 to 250 nm, respectively [42].

In the present work, we synthesized ZIF-8 materials with a wide range of crystal size through the ligand-excess approach. These materials were then milled with Fe(II) acetate and 1,10-phenanthroline to form catalyst precursors. The latter were pyrolyzed in Ar at 1050 °C, with a heating either in ramp or flash mode, to form Fe–N–C electrocatalysts. The structure and morphology of ZIF-8 powders, catalyst precursors and catalysts were investigated with SEM, X-ray diffraction and N_2 sorption while the Fe–N–C catalysts were electrochemically characterized in a single cell PEMFC.

2. Results and Discussion

2.1. Morphology and Size of ZIF-8 Nanocrystals

Figure 1 shows the SEM images for the five synthetic conditions of ZIF-8 (labelled hereafter as Z8) with ratios of 2-MeIm to Zn(II) (denoted as X hereafter) varying from 40 to 140 in the initial reagent solution. It is seen that the morphology of these Z8-X samples did not change with the molar ratio X, but the crystal size drastically decreased with increasing molar ratio. Crystals 1200–1800 nm in size are seen for Z8-40, 250–700 nm for Z8-60, 160–400 nm for Z8-80, 100–280 nm for Z8-100, and 80–200 nm for Z8-140. This agrees with the results reported by Kida *et al.* [42]. The vast majority of the crystals show a well-defined truncated rhombic dodecahedron morphology [42,44]. As a comparison, Figure 1 also shows a typical SEM image for Basolite®. A large dispersion size from 280–640 nm is observed, but most of the crystals are larger than 400 nm. The average size observed with Basolite® is similar to that of Z8-60 (Figure 1). Hence, the set of Z8 materials synthesized here forms an interesting basis to investigate the size effect of Z8 on the activity and performance of Fe–N–C catalysts that will be derived from them. Figure S1 shows the powder XRD patterns of the various Z8-X materials. All materials are well crystallized, even at the highest ratio of 2-MeIm to Zn(II) corresponding to the smallest crystals. All diffraction lines can be assigned to the sodalite topology of ZIF-8. Kida *et al.*, observed XRD peaks assigned to zinc hydroxides by-products at ratios of 2-MeIm to Zn(II) ≤ 20, peaks that were absent at molar ratios ≥40 [42]. In this work, we restricted ourselves to ratios ≥40 and the materials are thus phase-pure Z8 crystals. The accessibility of the cavities in these materials was then investigated with N_2 sorption (Figure S2). No hysteresis is observed and the isotherms have a type I shape, characteristic for microporous materials. The specific

surface area slightly decreases with decreasing Z8 crystal size (Table 1, 2nd column). For the smallest crystals (Z8-100 and 140), the isotherms show a sharp rise at high P/P_0, assigned to the filling of mesopores existing between ZIF crystals [42].

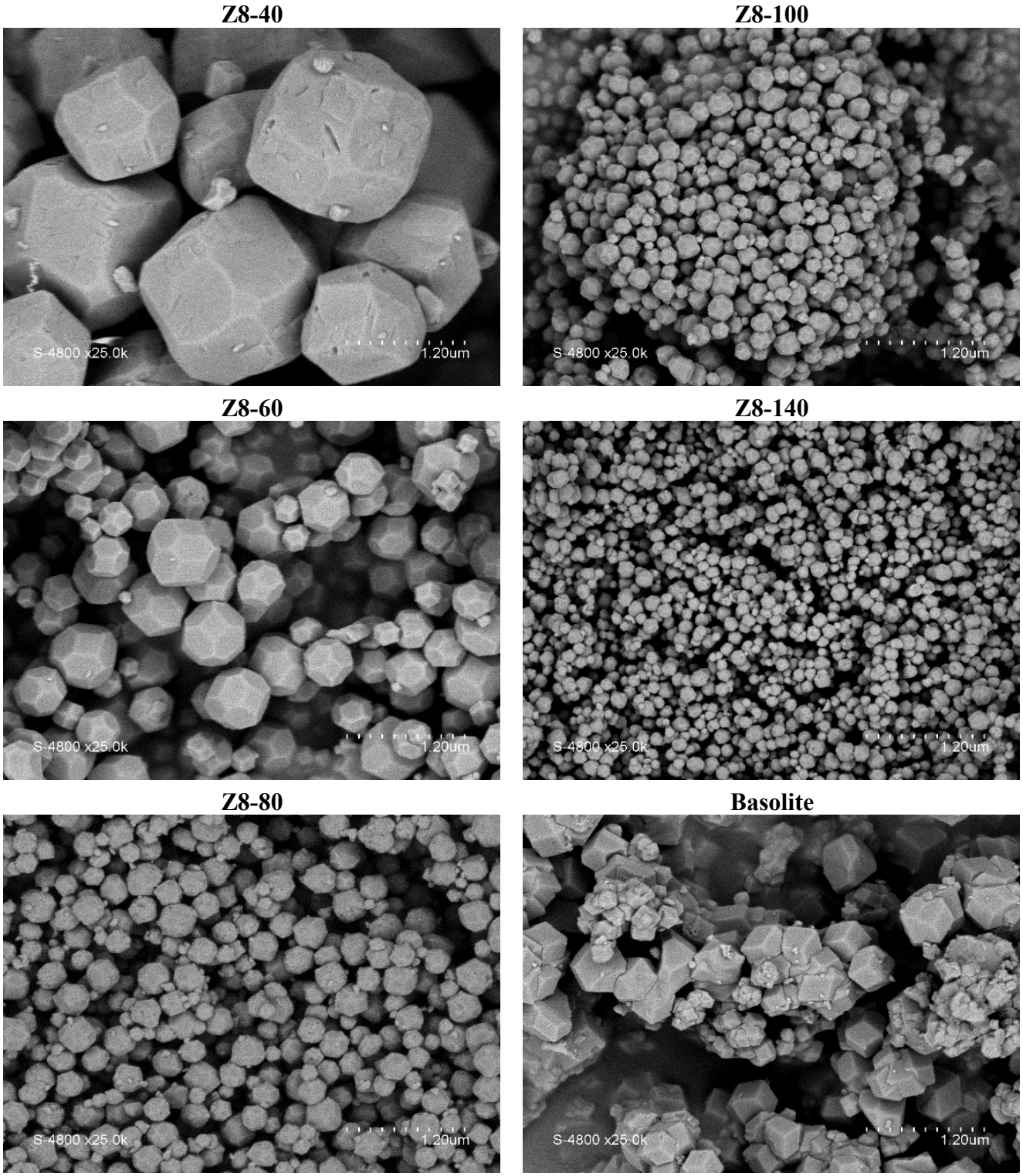

Figure 1. SEM micrographs of Z8-X crystals synthesized with the excess-ligand approach in aqueous solution at different molar ratios X of 2-MeIm to Zn(II), and SEM of the commercial Z8, Basolite®. The scale bar is 1.20 μm for all micrographs.

Table 1. BET specific areas of non-pyrolyzed and pyrolyzed materials.

Z8 Material	BET Specific Area/m^2 g^{-1}			
	as-synthesized Z8-X	Z8-X-400 rpm-F	Z8-X-100 rpm-F	Z8-X-100 rpm-R
Z8-40	1798	412	-	726
Z8-60	1767	372	-	745
Z8-80	1654	439	-	738
Z8-100	1543	412	367	673
Z8-140	1524	292	-	722
Basolite®	1618	357	-	719

2.2. Characterization of Fe–N–C Catalysts Obtained from Various ZIF-8 Materials without Templating

A first series of Fe–N–C catalysts was synthesized via flash pyrolysis in Ar of catalyst precursors prepared from Fe(II) acetate, phen and Z8-X materials. All catalyst precursors discussed in this sub-section were prepared by planetary milling the dry precursor powders at 400 rpm (see Section 3.2). These process parameters are those used by us previously [8,46]. An example of a catalyst label is Z8-40-400 rpm-F, indicating that Z8-40 was used, the milling speed was 400 rpm and the pyrolysis was carried out in flash mode. The SEM images of this first series of Fe–N–C catalysts are shown in Figure 2. Clearly, the morphology and size of the Fe–N–C catalytic particles are totally different from those of the starting Z8-X crystals. Even when starting from the largest Z8 crystals (Z8-40), most particles in Z8-40-400-F lost their original size (Figures 1 and 2). The visual impression is that the pristine Z8 batches with different average crystal size (100–1600 nm) resulted after milling at 400 rpm and flash pyrolysis in Fe–N–C agglomerates with a common size of *ca.* 300–600 nm, independent of the initial Z8 crystal size. It therefore seems that the largest Z8 crystals (Z8-40) are transformed into catalytic particles of a smaller size, while the smallest Z8 crystals (Z8-140) are transformed into larger catalytic particles.

Z8-40-400 rpm-F **Z8-100-400 rpm-F**

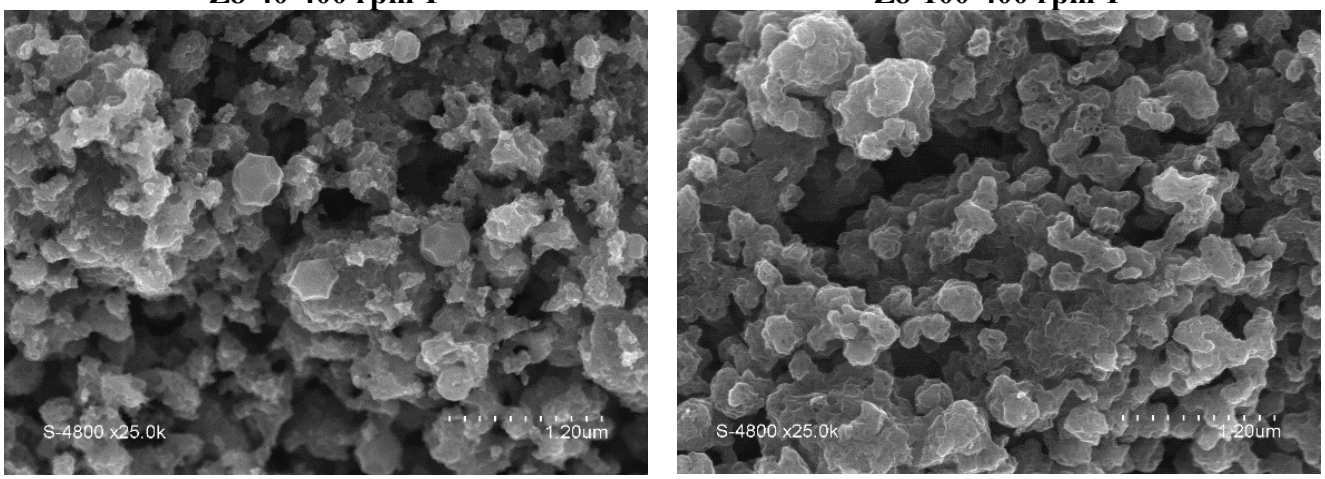

Figure 2. *Cont.*

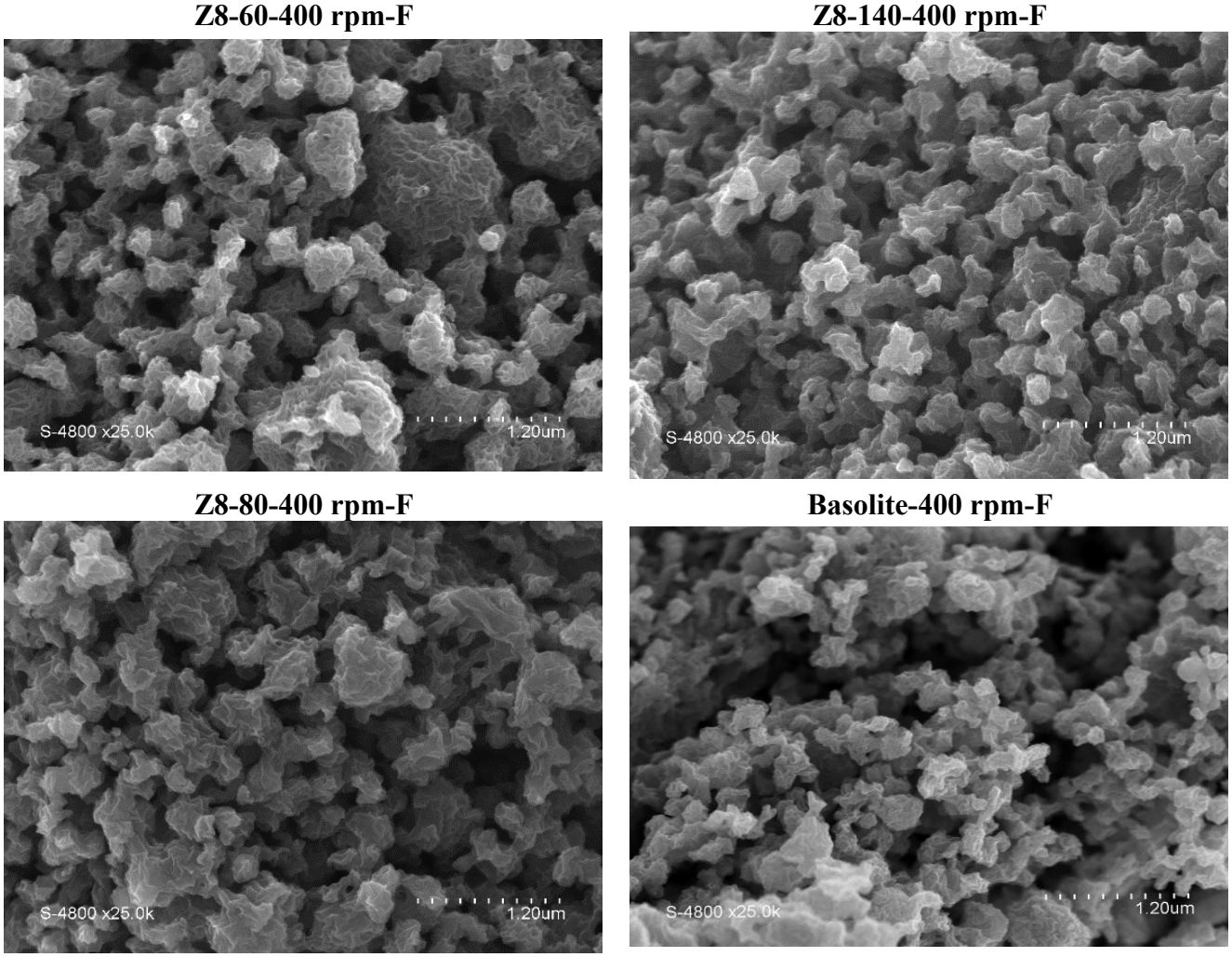

Figure 2. SEM micrographs of Fe–N–C catalysts derived from Fe(II), phen and Z8-X powders or Basolite®, ballmilled at 400 rpm and pyrolyzed at 1050 °C in Ar in flash mode. The scale bar is 1.20 μm for all SEM micrographs.

Figure S3 shows the N_2 isotherms for this series of catalysts, and Table 1 (3rd column) reports their BET areas. No clear trend is observed for the BET area. Figure 3 shows the PEMFC polarization curves recorded for a cathode loading of 4 mg cm^{-2} for this series of Fe–N–C catalysts. As seen in the inset of Figure 3, the ORR activity at 0.9 V iR-free is similar for all Z8-X-400 rpm-F samples (0.4–0.8 mA cm^{-2}) but lower than that of the Fe–N–C catalyst derived from Basolite® (1.5 mA cm^{-2}). The similar ORR activities and fuel cell performance obtained within this series agree with their similar morphology and specific surface area. The higher ORR activity obtained with Basolite® is possibly assigned to the presence of 100 ppm of iron atomically-dispersed in Basolite®. We will report on this in the near future.

In view of this first set of morphological and electrochemical results, we then investigated the effect of two process parameters that might explain the lack of templating observed on this first series of Fe–N–C catalysts. Those parameters are (i) the rotation rate applied during the ball milling of Fe(II), phen and Z8-X, and (ii) the heating mode. Previous works have recently reported on the templating of nano-ZIFs after pyrolysis in inert gas, but the heating mode was a ramp at 5 °C min^{-1} [35,36]. Our

flash pyrolysis mode is unusual but was found to be crucial in order to precisely control the pyrolysis duration, which is in turn important when pyrolyzing in reactive NH_3 atmosphere [7,20]. Precisely controlling the pyrolysis duration is however less important when the pyrolysis is carried out in inert gas since no continuous chemical reaction occurs between the formed carbonaceous material and inert gas.

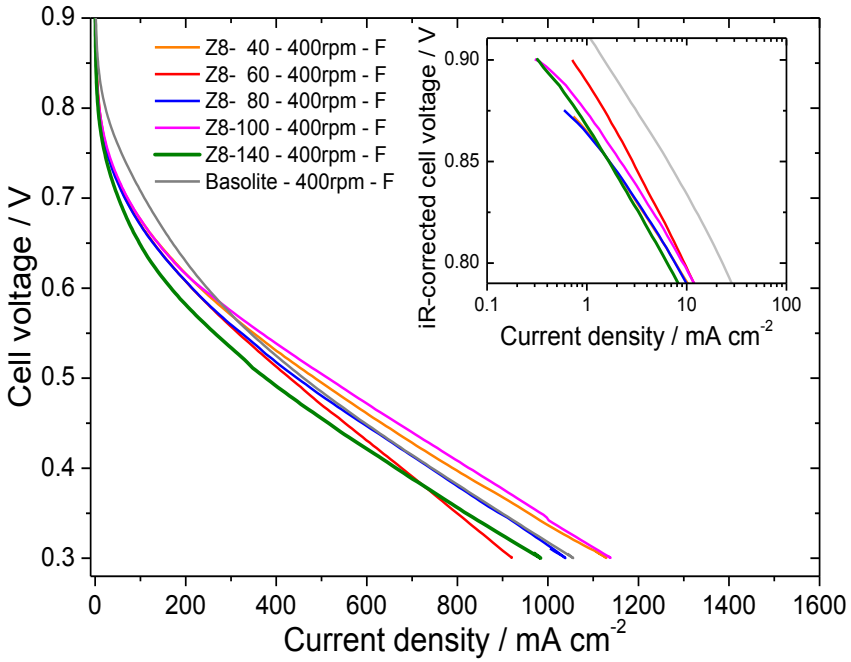

Figure 3. Non iR-corrected PEMFC polarization curves with cathodes comprising 4 mg cm^{-2} of Fe–N–C catalysts. Ballmilling was carried out at 400 rpm for forming catalyst precursors from Fe(II) acetate, phen and Z8-X powders. The catalyst precursors were subsequently pyrolyzed in flash mode. Inset: Tafel plots at high potential of the iR-corrected polarization curves.

2.3. Effects of Milling Speed and Heating Mode on the Morphology & Performance of Fe–N–C Catalysts

In this section, we selected Z8-100 to investigate the effects of milling speed (400 or 100 rpm) and heating mode (flash or ramp) on the morphology of Fe–N–C catalysts. Z8-100 was selected because its average crystal size is smaller than that of Basolite® and smaller than that of the agglomerates in the first series of Fe–N–C catalysts. The morphological changes of the materials were investigated with SEM at different stages of the synthesis. Fixing the milling speed at 400 rpm, the SEM images of (a) Z8-100, (b) the corresponding catalyst precursor ballmilled at 400 rpm and (c,d) the corresponding Fe–N–C catalysts after pyrolysis in flash or ramp mode are shown in Figure 4. Milling at 400 rpm leads to the formation of agglomerates that are larger than the pristine Z8-100 crystals (Figure 4b) and also leads to an amorphization of the catalyst precursor, as shown by XRD (Figure S4).

Following the milling step, the pyrolysis does not significantly modify the macroscopic morphology of those materials, regardless of whether the pyrolysis is carried out in flash or ramp mode (Figure 4c,d).

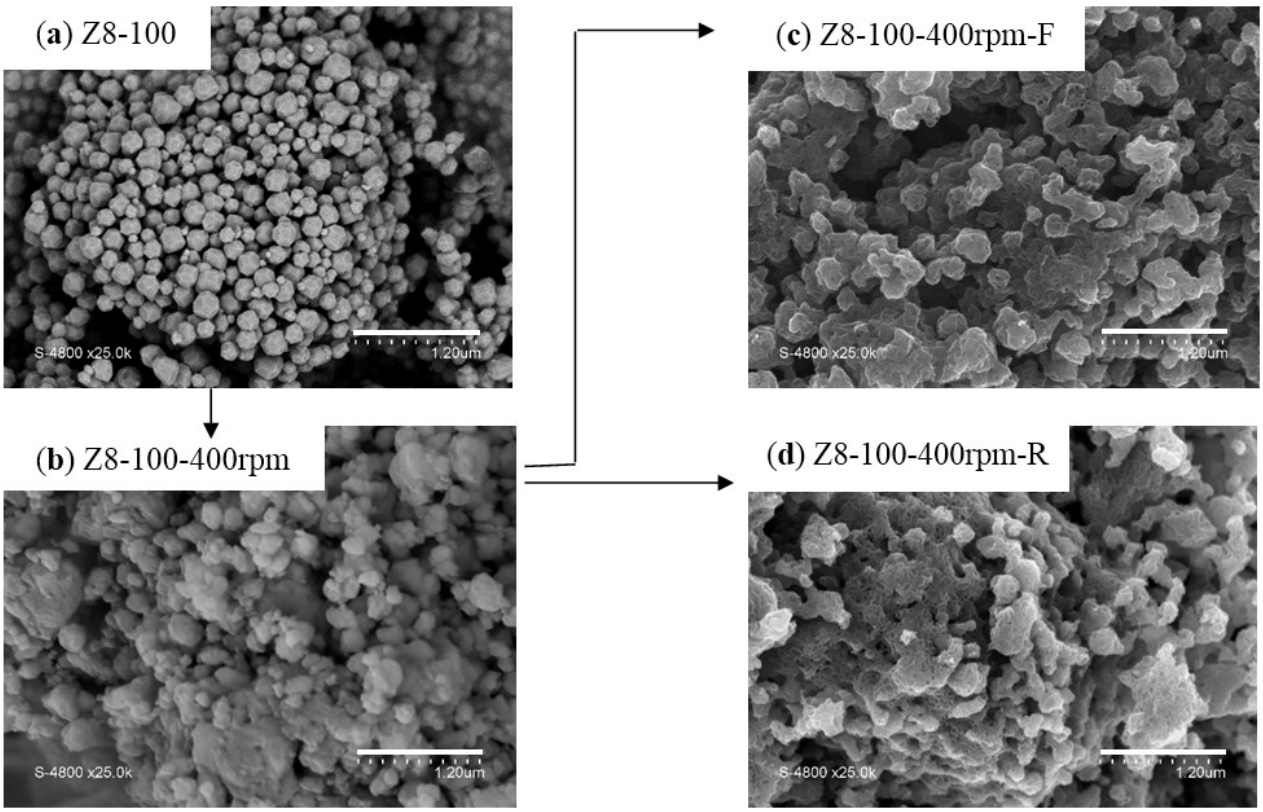

Figure 4. SEM micrographs of (**a**) Z8-100 crystals; (**b**) the catalyst precursor derived from Fe(II), phen and Z8-100 mixed via ballmilling at 400 rpm, and (**c**,**d**) Fe–N–C catalysts obtained by pyrolyzing that catalyst precursor at 1050 °C in Argon, either in flash (**c**) or ramp mode (**d**). The scale bar is 1.20 μm for all SEM micrographs.

The same investigation of morphological changes at different stages of synthesis was then carried out with a lowered milling speed of 100 rpm (Figure 5). The lowered milling speed not only preserved the original shape of Z8-100 crystals in the catalyst precursor but also prevented the formation of aggregates (Figure 5a,b). Moreover, powder X-ray diffraction confirmed that the lowered milling speed resulted in an X-ray diffractogram now superimposed with that of Z8-100 (Figure S4). It therefore seems that a correlation exists between crystallographic amorphization at high milling speed (XRD pattern) and the agglomeration observed on the SEM images of catalyst precursors. For various ZIFs and MOFs, it can thus be expected that the milling speed should be minimized to avoid amorphization during the milling stage. The threshold milling speed at which amorphization starts will likely depend on the mechanical properties of each specific MOF structure. Following the milling stage at 100 rpm, the macroscopic morphology of Z8-100 crystals is also maintained in the Fe–N–C catalyst after pyrolysis in flash or ramp mode (Figure 5c,d). With the latter pyrolysis mode, a well dispersed structure with spherical entities is observed, while in the case of the flash pyrolysis mode, the Fe–N–C catalytic particles seem to be elongated and slightly more interconnected or fused together (Figure 5c). Higher resolution SEM images better highlight such microscopic morphological and surface-roughness differences between Z8-100-100 rpm-F and Z8-100-100 rpm-R (Figure S5).

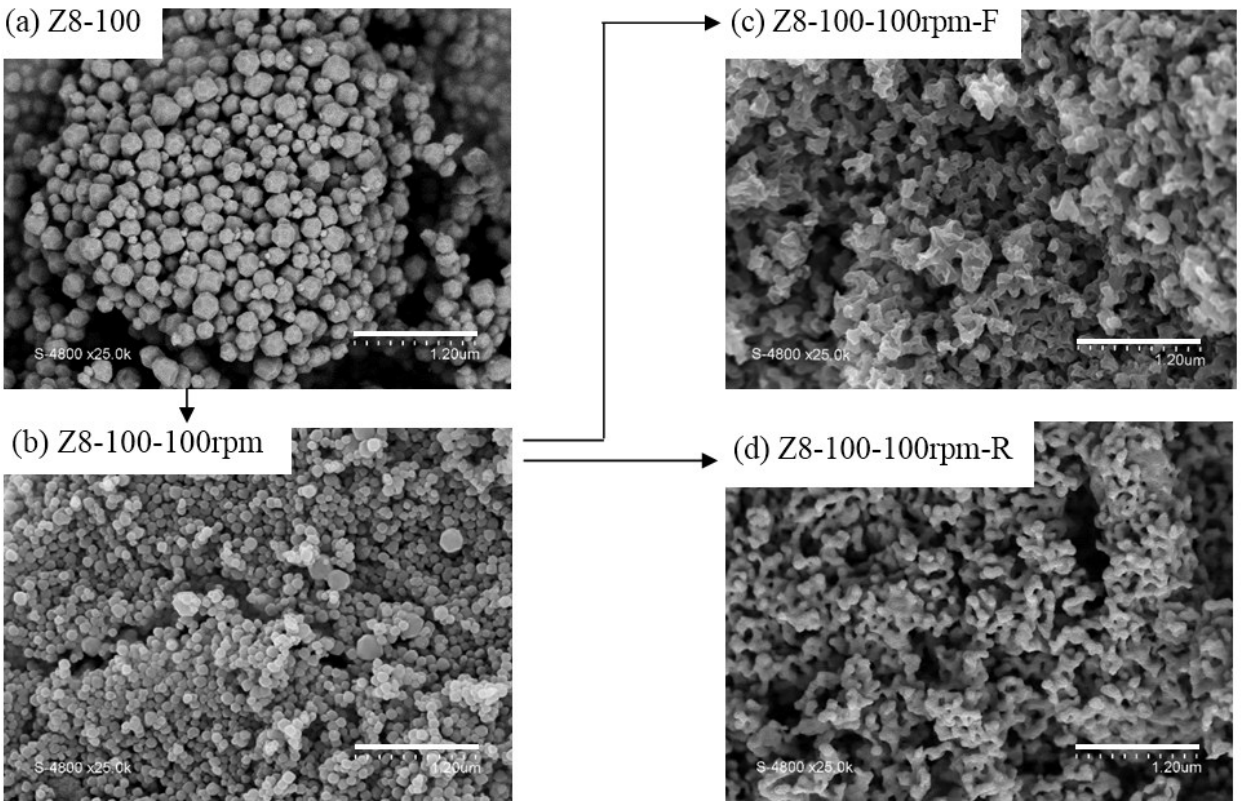

Figure 5. SEM micrographs of (**a**) Z8-100 crystals; (**b**) the catalyst precursor derived from Fe(II), phen and Z8-100 mixed via ballmilling at 100 rpm, and (**c**,**d**) Fe–N–C catalysts obtained by pyrolyzing that catalyst precursor at 1050 °C in Argon, either in flash (**c**) or ramp mode (**d**). The scale bar is 1.20 μm for all SEM micrographs.

A much more obvious difference is however observed in the BET areas of the two materials, 367 and 673 $m^2\ g^{-1}$ for Z8-100-100 rpm-F and Z8-100-100 rpm-R, respectively (Table 1). The twice higher uptake of N_2 at the initial stage of the isotherm ($P/P_0 < 0.02$) also indicates a much higher microporous surface area after a ramp pyrolysis (Figure S6). This major difference is interpreted as an increased accessibility of the intra-particular pores after a ramp pyrolysis, compared to the case with flash pyrolysis. It is proposed that the flash mode, implying a high gasification rate of Z8 (about 66% of the initial Z8 mass is gasified, probably during the first minute of pyrolysis), not only leads to the deformation of the templating Z8 crystals but also to the formation of closed pores within carbonized crystals. If the outer surface of Z8 crystals fuses or becomes less porous before the carbonization is completed in the depth of the crystals, this will impede or slow down the outgassing of volatile products formed within the crystals. Pressure increase within Z8 crystals under carbonization at the initial stage of a flash pyrolysis may also ensue, distorting the shape of the crystals and modifying the interconnections between the pores of the final pyrolysis product.

Figure 6 shows the PEMFC polarization curves recorded with a cathode loading of 4 mg cm^{-2} for the four Fe–N–C catalysts derived from Z8-100, and ballmilled at 400 or 100 rpm and pyrolyzed either in flash or ramp mode. As observed previously, the ORR activity at 0.9 V iR-free is low for the Fe–N–C catalyst prepared via milling at 400 rpm and pyrolyzed in flash mode, when compared to that of the catalyst derived from Basolite® (insets of Figures 3 and 6).

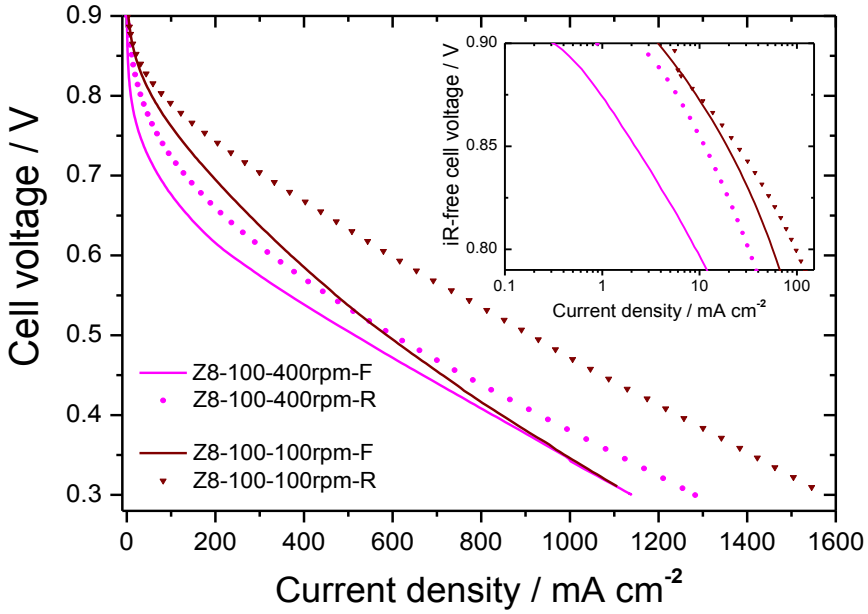

Figure 6. PEMFC polarization curves with cathodes comprising 4 mg cm^{-2} of Fe–N–C catalysts. Ballmilling was carried out at 400 or 100 rpm for forming catalyst precursors from Fe(II) acetate, phen and Z8-100, catalyst precursors that were subsequently pyrolyzed in flash (F) or ramp mode (R). Inset: Tafel plots at high potential of the iR-corrected polarization curves.

The ORR activity at 0.9 V iR-free is however enhanced by a factor of seven when the heating mode is switched to ramp (magenta solid to magenta dotted curve in the inset of Figure 6). The corresponding enhancement of the current density at 0.5 V is however minor (magenta curves in Figure 6), probably due to the formation of large agglomerates during the milling at 400 rpm. Even higher ORR activities are observed for the two Fe–N–C catalysts derived from Z8-100 and prepared via milling at 100 rpm, then pyrolyzed in flash or ramp mode (inset of Figure 6, brown curves). The ORR activities at 0.9 V iR-free of those two catalysts are now significantly higher than that observed with the Fe–N–C catalyst derived from Basolite® via 400 rpm milling and flash pyrolysis (3.7 and 5.3 mA cm^{-2} *vs.* 1.5 mA cm^{-2}). Even more interesting, the combined low milling speed of 100 rpm with the ramped pyrolysis mode results in a much improved performance at lower cell voltage, reaching 910 mA cm^{-2} at 0.5 V (Figure 6), instead of 374–515 mA cm^{-2} for the first series of Fe–N–C catalysts synthesized with 400 rpm milling speed and flash pyrolysis (Figure 3). The beneficial effect of a combined low milling speed (100 rpm) with a ramp pyrolysis mode is obvious at 0.5 V, compared to the 100 rpm milling speed combined with a flash pyrolysis (910 *vs.* 585 mA cm^{-2}, brown curves in Figure 6). The high ORR activity at 0.9 V but medium performance at 0.5 V of Z8-100-100 rpm-F was reproducible. Hence, the catalytic sites are more accessible by O_2 in Z8-100-100 rpm-R and this can be correlated to its higher BET area. While Z8-100-100 rpm-F shows a particle size similar to that in Z8-100-100 rpm-R (Figure 5c,d), the intra-particle pore network is less developed (lower BET area, Table 1) and less microporous (Figure S6).

2.4. Characterization of Fe–N–C Catalysts Templated from Various ZIF-8 Materials

In view of the templating effect and positive electrochemical result obtained with Z8-100-100 rpm-R, the synthesis parameters were then fixed (milling speed 100 rpm and ramp pyrolysis) and the investigation of the templating effect for the different Z8 materials shown in Figure 1 is now possible. The BET areas for this second series of Fe–N–C materials are reported in Table 1 (5th column). In this second series of catalysts, all BET areas are significantly higher than those measured for the first series of Fe–N–C catalysts (Table 1, 3rd column). High BET and microporous area is required for reaching a high ORR activity at high potential. This is demonstrated by the high ORR activity observed for all materials within this second series of Fe–N–C catalysts (inset of Figure 7).

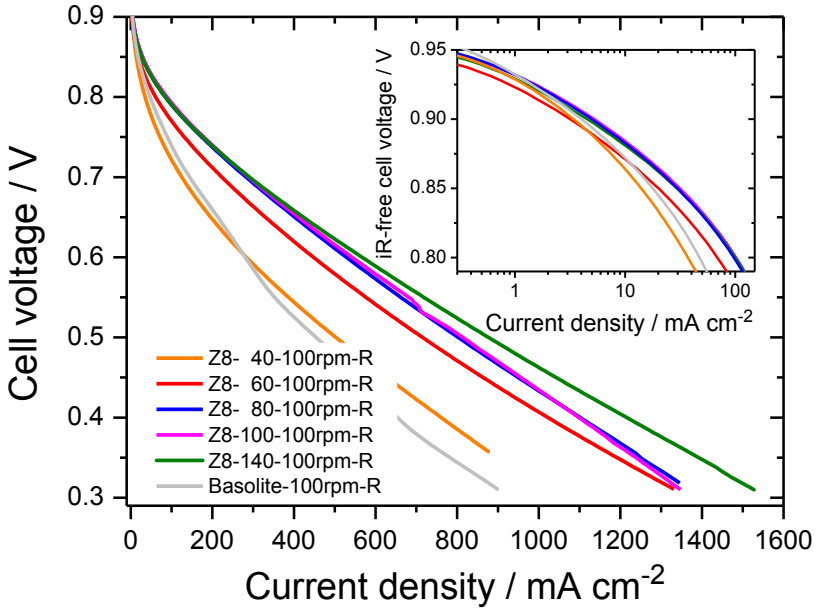

Figure 7. Non-iR corrected PEMFC polarization curves with cathodes comprising 4 mg cm^{-2} of Fe–N–C catalysts. Ballmilling was carried out at 100 rpm for forming catalyst precursors from Fe(II) acetate, phen and Z8-X powders. The catalyst precursors were heated in ramp mode. Inset: Tafel plots at high potential of iR-free polarization curves (the green curve is superimposed below the blue and magenta curves).

Beyond the fact that the average BET areas of these two series of catalysts differ, the N_2 sorption isotherms also reveal the presence of a hysteresis for the materials pyrolyzed with flash mode, but little or no hysteresis for the materials pyrolyzed with ramp mode (Figures S7 and S8). This is interpreted as a less tortuous path and the absence of bottlenecks in the intra-particle pore network of materials pyrolyzed in ramp mode. The ORR activity at 0.9 V iR-free is high and quite homogeneous within this second series of Fe–N–C catalysts (3.2–5.3 mA cm^{-2}, see inset of Figure 7), in agreement with their similar BET areas and N_2 isotherms (Table 1, Figure S7). Hence, the size of Z8 crystals before pyrolysis does not play a major role regarding the ORR activity after pyrolysis. However, the effect of Z8 particle size (and thus of Fe–N–C catalytic particle size after pyrolysis, due to the templating observed earlier for Z8-100) is obviously demonstrated in the linear *E vs. I* plots, showing a continuous

increase of the current density at e.g., 0.5 V with decreased Z8 particle size (Figure 7). The clear assignment of the increased performance at 0.5 V to the reduced catalytic particle size is made possible due to the very similar ORR activities observed at 0.9 V for this second series of catalysts. This synthesis approach therefore allows a control of the particle size and quality of the intra-particle porous network in Fe–N–C catalysts derived from the pyrolysis of metal-organic frameworks.

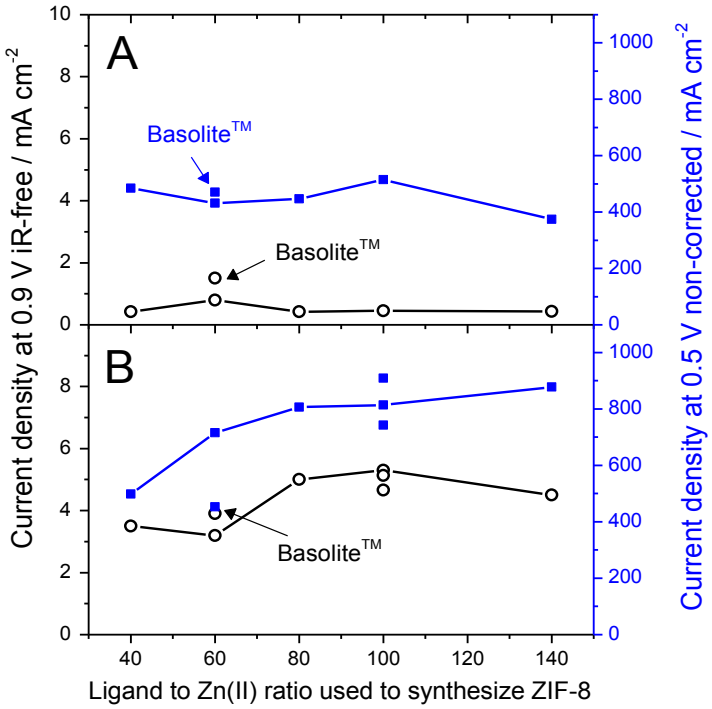

Figure 8. (**a**) Current density at 0.9 V iR-free and 0.5 V against the ligand-to-Zn(II) ratio used for the synthesis of Z8 samples. The catalysts were synthesized with 400 rpm milling and flash pyrolysis; (**b**) the same figure for catalysts synthesized with 100 rpm milling and ramp pyrolysis. Basolite® is artificially positioned at a ligand-to-Zn(II) ratio of 60.

Figure 8 summarizes the ORR activity at 0.9 V iR-free cell voltage (left handside *Y*-axis) and current density at 0.5 V uncorrected voltage (right handside *Y*-axis) for the two series of Fe–N–C catalysts. The *X*-axis reports the ligand to Zn(II) ratio used for synthesizing Z8 materials, and is thus inversely correlated with the average crystal size of Z8 materials. In this figure, the results obtained with Basolite® are also shown. In order to do this, Basolite® was artificially attributed a ratio of ligand-to-Zn(II) of 60, on the basis of similar Z8 crystals size observed for Z8-60 and Basolite® (Figure 1). For Z8-100-100 rpm-R, the reproducibility of the results was verified on three different MEAs (Figure 8B). The best MEA reached 910 mA cm^{-2} at 0.5 V cell voltage and a peak power density of 500 mW cm^{-2} at 0.39 V (Figure 6, brown dotted curve). This result surpasses by a factor of two the current density at 0.5 V previously obtained with Basolite® and with our typical process parameters (400 rpm, flash pyrolysis in Ar, Figure 8A) [46]. The initial peak power density of 500 mW cm^{-2} is among the highest reported for Fe–N–C catalysts, including those pyrolyzed in NH_3 [8–10,12,26,27,30,47]. This is particularly interesting since such Fe–N–C catalysts pyrolyzed in inert gas are intrinsically more stable than NH_3-pyrolyzed Fe–N–C catalysts [8]. While the crystal size of ZIF-8 may be further decreased, this might not necessarily lead to further increased performance

since other transport phenomena may then become limiting (proton conduction and O_2 diffusion across the cathode layer, rather than O_2 diffusion in single catalytic particles). The present work also clearly demonstrates that the desired pore network for a well-performing Fe–N–C catalyst is highly microporous, and with no hysteresis attributed to small mesopores or bottlenecks (Figure S8). The durability of such templated Ar-pyrolyzed Fe–N–C catalysts with improved initial performance will be investigated in the near future. The effect of even higher pyrolysis temperature in inert gas (1080–1150 °C) will also be investigated with this approach, since a beneficial effect on the durability was recently reported for non-templated Fe–N–C catalysts derived from Basolite® [30].

3. Experimental Section

3.1. Synthesis of Nanosized ZIF-8 Crystals

Phase pure ZIF-8 crystals were synthesized at room temperature in aqueous solution according to the report by Kida and coworkers [42]. The size of ZIF-8 crystals was controlled with the molar ratio of 2-methylimidazole to Zn(II) nitrate hexahydrate. For example, to reach a ratio of 60, a mass of 0.744 g of Zn(II) nitrate hexahydrate (2.5 mmol) was dissolved in 10 mL of deionized water and added to a solution consisting of 12.3 g of 2-MeIm (150 mmol) previously dissolved in 90 mL of deionized water. The final molar composition of this reagent solution is 1:60:2228 for Zn(II):2-MeIm:water. The solution was constantly stirred and quickly turned cloudy and a suspension was obtained. Twenty-four hours later, the suspension was centrifuged at 11,000 rpm for 15 min, washed with methanol and re-dispersed with ultrasounds. The centrifugation and re-dispersion step was repeated three times. The product was then vacuum-dried for 24 h at 80 °C. In order to obtain ZIF-8 crystals with different sizes, the ratio 2-MeIm:Zn was adjusted to different values (40, 60, 80, 100, 140) by adjusting the amount of 2-MeIm while keeping the amount of the Zinc salt and of water constant. The resulting ZIF-8 materials are labelled Z8-X, with X being the ratio of 2-MeIm:Zn.

3.2. Synthesis of Fe–N–C Catalysts

All catalyst precursors were prepared via the dry ballmilling of ZIF-8 nanocrystals, Fe(II) acetate and 1,10-phenanthroline [32]. Then, 32.45 mg Fe(II)Ac, 100 mg of 1,10-phenanthroline and 800 mg of ZIF-8 were weighed and poured into a ZrO_2 crucible. This corresponds to 1 wt. % Fe in the catalyst precursor before pyrolysis. Hundred zirconium-oxide balls of 5 mm diameter were then added. The ZrO_2 crucible was then sealed under air and placed in a planetary ball-miller (Fritsch Pulverisette 7 Premium, Fritsch, Idar-Oberstein, Germany). The powders were milled during 4 cycles of 30 min, at either 400 or 100 rpm milling speed. The catalyst precursors resulting from the milling were pyrolyzed at 1050 °C in flowing Ar for 1 h, via either a heat-chock procedure previously described by us [20], or via a ramp mode with a heating rate of 5 °C min^{-1}. For the latter, the catalyst dwell time at 1050 °C in Ar was also 1 h. Last, the obtained powders were ground in an agate mortar. The mass loss during pyrolysis due to Zn, C and N volatile compounds from ZIF-8 and phenanthroline was *ca.* 60–65 wt. %, leading to Fe contents of 2.5–2.9 wt. % in the final catalysts. The catalysts are labelled Z8-X-Yrpm-Z, where X is the ratio of ligand to Zn(II) used during ZIF-8 synthesis, Y is the rotation rate during milling of the catalyst precursor (100 or 400 rpm) and Z is the heating mode (F for flash pyrolysis and R for ramp

mode). For example, Z8-60-400 rpm-F corresponds to a catalyst precursor made from Fe, phen and Z8-60, milled at 400 rpm, and pyrolyzed in argon for 1 h with flash mode.

3.3. Material Characterization

The crystalline structure of ZIF-8 materials was investigated with X-ray diffraction using a PANanalytical X'Pert Pro powder X-ray diffractometer (Almelo, The Netherlands). The Brunauer–Emmett–Teller (BET) surface area and pore volume were measured with N_2 sorption at liquid nitrogen temperature (77 K) using a Micromeritics ASAP 2020 instrument (Norcross, GA, USA). Samples were degassed at 200 °C for 5 h in flowing nitrogen prior to measurements to remove guest molecules. The microstructure of ZIF-8 and Fe–N–C materials was investigated with SEM (Hitachi S-4800, Hitachi, Tokyo, Japan) after gold metallization.

3.4. Electrochemical Characterization

Electrochemical activity towards the ORR and initial power performance of the catalysts was determined in a single-cell laboratory fuel cell. The inks for the cathode electrode were prepared using the formulation of 20 mg of catalyst, 652 μL of an alcohol-based 5 wt. % Nafion® solution that also contains 15%–20% water, 326 μL of ethanol and 272 μL of de-ionized water. The inks were first sonicated, then agitated with a vortex mixer. These sonication-agitation steps were repeated every 15 min for a total duration of 1 h. Then, three aliquots of 405 μL of the cathode catalyst ink were deposited on the microporous layer of a commercial gas diffusion layer (Sigracet S10-BC, 4.48 cm^2, SGL Group The Carbon Company, Wiesbaden, Germany). The gas diffusion layer was heated on a heating plate to facilitate solvent evaporation, and the second and third aliquots were deposited only when the first and second aliquots had dried, respectively, in order to avoid layer cracking. This resulted in a total cathode catalyst loading of 4 mg cm^{-2}. The remaining solvents and water were then completely evaporated at 80 °C. The anode was a 0.5 $mg_{Pt} \cdot cm^{-2}$ electrode pre-deposited on Sigracet S10-BC. Membrane-electrode-assemblies were fabricated by hot-pressing the anode and cathode with geometric areas of 4.84 cm^2 against a Nafion® NRE-211 membrane at 135 °C for 2 min. The membrane electrode assemblies were installed in a single-cell PEMFC with serpentine flow fields (Fuel Cell Technologies Inc., Albuquerque, NM, USA). The fuel cell bench was an in-house bench connected to a Biologic Potentiostat with a 50 amperes booster. The experiments were controlled with the EC-Lab software (Bio-Logic Science Instruments, Claix, France). For all fuel cell tests reported in the present work, the cell temperature was 80 °C, the humidifier's temperature was 85 °C, and the inlet gas pressures were 1 bar gauge at both the anode and the cathode. The humidified H_2 and O_2 flow rates were *ca.* 50–70 sccm, as controlled downstream of the fuel cell. The fuel cell polarization curves were recorded with EC lab software using the cycling voltammetry experiment and scanning the cell at 0.5 $mV \cdot s^{-1}$.

4. Conclusions

The templating of nano-sized ZIF-8 crystals into catalytic Fe–N–C particles with open porosity is shown to result in improved power performance at high current density in PEM fuel cells. In order to

achieve a templating effect in the pyrolyzed catalysts, the milling speed used to mix the iron salt, phenanthroline and ZIF-8 precursors before pyrolysis is lowered to avoid agglomeration. In a second stage, the heating mode used to pyrolyze the catalyst precursors under inert gas is crucial in order to reach high BET and microporous areas and an intra-particle pore-network free of bottlenecks. A flash pyrolysis mode (room temperature to 1050 °C in circa 1.5 min) resulted in a low BET area and large hysteresis in the N_2 sorption isotherms while a ramp heating mode at 5 °C min^{-1} resulted in a high BET area and little or no hysteresis in the N_2 sorption isotherms. The use of ZIF-8 nanocrystals of average size 100 nm combined with a low milling speed for preparing the catalyst precursor that was subsequently pyrolyzed in argon in ramp mode resulted in a much improved ORR activity at high potential and also improved power performance at 0.5 V. The synthesis of Fe–N–C catalysts pyrolyzed in inert atmosphere and demonstrating improved power performance is important due to their known better durability in PEM fuel cells compared to NH_3-pyrolyzed Fe–N–C catalysts. The templating and open porosity effects resulting in improved power performance reported here for ZIF-8 will most likely be applicable to other MOFs as well and also open the door to the design of advanced composite materials comprising MOFs and corrosion-resistant supports such as carbon nanotubes or fibers.

Acknowledgments

We acknowledge funding from Agence Nationale de la Recherche, ANR, contract 2011 CHEX 004 01. The authors thank Didier Cot (Institut Européen des Membranes, Montpellier) for his contribution to the SEM measurements.

Author Contributions

Julien Hannauer synthesized and characterized nano ZIFs. Vanessa Armel synthesized and characterized Fe–N–C catalysts. Frédéric Jaouen supervised the research. Vanessa Armel and Frédéric Jaouen wrote the manuscript.

Conflicts of Interest

The authors declare no conflict of interest.

References

1. Debe, M. Electrocatalyst approaches and challenges for automotive fuel cells. *Nature* **2012**, *486*, 43–51.
2. Wagner, F.T.; Lakshmanan, B.; Mathias, M.F. Electrochemistry and the future of the automobile. *J. Phys. Chem. Lett.* **2010**, *1*, 2204–2219.
3. Resnick, P.R. A short history of Nafion. *Actual. Chim.* **2006**, *301*, 144–147.
4. Banerjee, S.; Curtin, D.E. Nafion® perfluorinated membranes in fuel cells. *J. Fluor. Chem*. **2004**, *125*, 1211.
5. Gasteiger, H.A.; Panels, J.E.; Yan, S.G. Dependence of PEM fuel cell performance on catalyst loading. *J. Power Sources* **2004**, *127*, 162–171.

6. Jaouen, F.; Proietti, E.; Lefèvre, M.; Chenitz, R.; Dodelet, J.-P.; Wu, G.; Chung, H.T.; Johnston, C.M.; Zelenay, P. Recent advances in non-precious metal catalysis for oxygen reduction reaction in polymer electrolyte fuel cells. *Energy Environ. Sci.* **2011**, *4*, 114–130.
7. Lefèvre, M.; Proietti, E.; Jaouen, F.; Dodelet, J.P. Iron-based catalysts with improved oxygen reduction activity in polymer electrolyte fuel cells. *Science* **2009**, *324*, 71–74.
8. Proietti, E.; Jaouen, F.; Lefèvre, M.; Larouche, N.; Tian, J.; Herranz, J.; Dodelet, J.-P. Iron-based cathode catalyst with enhanced power density in polymer electrolyte membrane fuel cells. *Nat. Commun*. **2011**, *2*, 416.
9. Wu, G.; More, K.L.; Johnston, C.M.; Zelenay, P. High-performance electrocatalysts for oxygen reduction derived from polyaniline, iron, and cobalt. *Science* **2011**, *332*, 443–447.
10. Zhao, D.; Shui, J.-L.; Grabstanowicz, L.R.; Chen, C.; Commet, S.M.; Xu, T.; Lu, J.; Liu, D.-J. Highly Efficient Non-Precious Metal Electrocatalysts Prepared from One-Pot Synthesized Zeolitic Imidazolate Frameworks. *Adv. Mater.* **2014**, *26*, 1093–1097.
11. Chang, S.-T.; Wang, C.-H.; Du, H.-Y.; Hsu, H.-C.; Kang, C.-M.; Chen, C.-C.; Wu, J.C.S.; Yen, S.-C.; Huang, W.-F.; Chen, L.-C.; *et al.* Vitalizing fuel cells with vitamins: Pyrolyzed vitamin B12 as a non-precious catalyst for enhanced oxygen reduction reaction of polymer electrolyte fuel cells. *Energy Environ. Sci.* **2012**, *5*, 5305–5314.
12. Serov, A.; Artyushkova, K.; Atanassov, P. Fe–N–C Oxygen Reduction Fuel Cell Catalyst Derived from Carbendazim: Synthesis, Structure, and Reactivity. *Adv. Energy Mater.* **2014**, *4*, 1301735.
13. Ma, S.; Goenaga, G.A.; Call, A.V.; Liu, D.J. Cobalt imidazolate framework as precursor for oxygen reduction electrocatalysts. *Chem. Eur. J*. **2011**, *17*, 2063–2067.
14. Jaouen, F.; Dodelet, J.P. Average turn-over frequency of O_2 electro-reduction for Fe/N/C and Co/N/C catalysts in PEFCs. *Electrochim. Acta* **2007**, *52*, 5975–5984.
15. He, P.; Lefèvre, M.; Faubert, G.; Dodelet, J.P. Oxygen reduction catalysts for polymer electrolyte fuel cells from the pyrolysis of various transition metal acetates adsorbed on 3,4,9,10-perylenetetracarboxylic dianhydride. *J. New Mater. Electrochem. Syst.* **1999**, *2*, 243–251.
16. Wu, G.; Johnston, C.M.; Mack, N.H.; Artyushkova, K.; Ferrandon, M.; Nelson, M.; Lezama-Pacheco, J.S.; Conradson, S.D.; More, K.L.; Myers, D.J.; *et al.* Synthesis-structure-performance correlation for polyaniline-Me-C non-precious metal cathode catalysts for oxygen reduction in fuel cells. *J. Mater. Chem.* **2011**, *21*, 11392–11405.
17. Lefèvre, M.; Dodelet, J.P. Recent advances in non-precious metal electrocatalysts for oxygen reduction in PEM fuel cells. *Electrochem. Soc. Trans.* **2012**, *45*, 35–44.
18. Charreteur, F.; Jaouen, F.; Dodelet, J.P. Iron porphyrin-based cathode catalysts for PEM fuel cells: Influence of pyrolysis gas on activity and stability. *Electrochim. Acta* **2009**, *54*, 6622–6630.
19. Kramm, U.I.; Herrmann-Geppert, I.; Fiechter, S.; Zehl, G.; Zizak, I.; Dorbandt, I.; Schmeißer, D.; Bogdanoff, P. Effect of iron-carbide formation on the number of active sites in Fe–N–C catalysts for the oxygen reduction reaction in acidic media. *J. Mater. Chem. A* **2014**, *2*, 2663–2670.
20. Jaouen, F.; Lefèvre, M.; Dodelet, J.P.; Cai, M. Heat-Treated Fe/N/C Catalysts for O_2 Electroreduction: Are Active Sites Hosted in Micropores? *J. Phys. Chem. B* **2006**, *110*, 5553–5558.

21. Jaouen, F.; Herranz, J.; Lefèvre, M.; Dodelet, J.P.; Kramm, U.I.; Herrmann, I.; Bogdanoff, P.; Maruyama, J.; Nagaoka, T.; Garsuch, A.; *et al.* Cross-laboratory experimental study of non-noble-metal electrocatalysts for the oxygen reduction reaction. *Appl. Mater. Interf.* **2009**, *1*, 1623–1639.
22. Ferrandon, M.; Kropf, A.J.; Myers, D.J.; Artyushkova, K.; Kramm, U.; Bogdanoff, P.; Wu, G.; Johnston, C.M.; Zelenay, P. Multitechnique characterisation of a polyaniline-iron-carbon oxygen reduction catalyst. *J. Phys. Chem. C* **2012**, *116*, 16001–16013.
23. Park, K.S.; Ni, Z.; Côté, A.P.; Choi, J.Y.; Huang, R.; Uribe-Romo, F.J.; Chae, H.K.; O'Keeffe, M.; Yaghi, O.M. Exceptional chemical and thermal stability of zeolitic imidazolate frameworks. *Proc. Natl. Acad. Sci. USA* **2006**, *103*, 10186–10191.
24. Wu, H.; Zhou, W.; Yildirim, T. Hydrogen Storage in a Prototypical Zeolitic Imidazolate Framework-8. *J. Am. Chem. Soc.* **2007**, *129*, 5314–5315.
25. Tian, J.; Morozan, A.; Sougrati, M.T.; Lefèvre, M.; Chenitz, R.; Dodelet, J.-P.; Jones, D.; Jaouen, F. Optimized Synthesis of Fe/N/C Cathode Catalysts for PEM Fuel Cells: A Matter of Iron—Ligand Coordination Strength. *Angew. Chem. Int. Ed.* **2013**, *52*, 6867–6870.
26. Strickland, K.; Miner, E.; Jia, Q.; Tylus, U.; Ramaswamy, N.; Liang, W.; Sougrati, M.-T.; Jaouen, F.; Mukerjee, S. Highly active oxygen reduction non-platinum group metal electrocatalyst without direct metal-nitrogen coordination. *Nat. Commun.* **2015**, *6*, 7343.
27. Barkholtz, H.M.; Chong, L.; Kaiser, Z.B.; Xu, T.; Liu, D.J. Highly Active Non-PGM Catalysts Prepared from Metal Organic Frameworks. *Catalysts* **2015**, *5*, 955–965.
28. Herranz, J.; Jaouen, F.; Lefèvre, M.; Kramm, U.I.; Proietti, E.; Dodelet, J.-P.; Bogdanoff, P.; Fiechter, S.; Abs-Wurmbach, I.; Bertrand, P.; *et al.* Unveiling N-protonation and anion-binding effects on Fe/N/C catalysts for O_2 reduction in proton-exchange-membrane fuel cells. *J. Phys. Chem. C* **2011**, *115*, 16087–16097.
29. Larouche, N.; Chenitz, R.; Lefèvre, M.; Proietti, E.; Dodelet, J.P. Activity and stability in proton exchange membrane fuel cells of iron-based cathode catalysts synthesized with addition of carbon fibers. *Electrochim. Acta* **2014**, *115*, 170–182.
30. Yang, L.; Larouche, N.; Chenitz, R.; Zhang, G.; Lefèvre, M.; Dodelet, J.-P. Activity, performance, and durability of for the reduction of oxygen in PEM fuel cells, of Fe/N/C electrocatalysts obtained from the pyrolysis of metal-organic-framework and iron porphyrin precursors. *Electrochim. Acta* **2015**, *159*, 184–197.
31. Wu, G.; Artyushkova, K.; Ferrandon, M.; Kropf, A.J.; Myers, D.; Zelenay, P. Performance durability of polyaniline-derived non-precious cathode catalysts. *Electrochem. Soc. Trans.* **2009**, *25*, 1299–1311.
32. Goellner, V.; Baldizzone, C.; Schuppert, A.; Sougrati, M.T.; Mayrhofer, K.; Jaouen, F. Degradation of Fe/N/C catalysts upon high polarization in acid medium. *Phys. Chem. Chem. Phys.* **2014**, *16*, 18454–18462.
33. Kramm, U.I.; Lefèvre, M.; Larouche, N.; Schmeisser, D.; Dodelet, J.P. Correlations between mass activity and physicochemical properties of Fe/N/C catalysts for the ORR in PEM fuel cell via ^{57}Fe Mössbauer spectroscopy and other techniques. *J. Am. Chem. Soc.* **2013**, *136*, 978–985.

34. Morozan, A.; Sougrati, M.T.; Goellner, V.; Jones, D.; Stievano, L.; Jaouen, F. Effect of Furfuryl Alcohol on Metal Organic Framework-based Fe/N/C Electrocatalysts for Polymer Electrolyte Membrane Fuel Cells. *Electrochim. Acta* **2014**, *119*, 192–205.
35. Xia, W.; Zhu, J.; Guo, W.; An, L.; Xia, D.; Zou, R. Well-defined carbon polyhedrons prepared from nano metal-organic frameworks for oxygen reduction. *J. Mater. Chem. A* **2014**, *2*, 11606–11613.
36. Zhang, L.; Su, Z.; Jiang, F.; Yang, L.; Qian, J.; Zhou, Y.; Li, W.; Hong, M. Highly graphitized nitrogen-doped porous carbon nanopolyhedra derived from ZIF-8 nanocrystals as efficient electrocatalysts for oxygen reduction reactions. *Nanoscale* **2014**, *6*, 6590–6602.
37. Cravillon, J.; Münzer, S.; Lohmeier, S.-J.; Feldhoff, A.; Huber, K.; Wiebcke, M. Rapid room-temperature synthesis and characterization of nanocrystals of a prototypical zeolitic imidazolate framework. *Chem. Mater.* **2009**, *21*, 1410–1412.
38. Zacher, D.; Nayuk, R.; Schweins, R.; Fischer, R.A.; Huber, K. Monitoring the Coordination Modulator Shell at MOF Nanocrystals. *Crystal Growth Design* **2014**, *14*, 4859–4863.
39. Sindoro, M.; Yanai, N.; Jee, A.-J.; Granick, S. Colloidal-Sized Metal Organic Frameworks: Synthesis and Applications. *Acc. Chem. Res.* **2014**, *47*, 459–469.
40. Fan, X.; Wang, W.; Li, W.; Zhou, J.; Wang, B.; Zheng, J.; Li, X. Highly Porous ZIF-8 Nanocrystals Prepared by a Surfactant Mediated Method in Aqueous Solution with Enhanced Adsorption kinetics. *ACS Appl. Mater. Interf.* **2014**, *6*, 14994–14999.
41. Diring, S.; Furukawa, S.; Takashima, Y.; Tsuruoka, T.; Kitagawa, S. Controlled Multiscale Synthesis of Porous Coordination Polymer in Nano/Micro Regimes. *Chem. Mater.* **2010**, *22*, 4531–4538.
42. Kida, K.; Okita, M.; Fujita, K.; Tanaka, S.; Miyake, Y. Formation of high crystalline ZIF-8 in an aqueous solution. *CrystEngComm* **2013**, *15*, 1794–1801.
43. Tsuruoka, T.; Furukawa, S.; Takashima, Y.; Yoshida, K.; Isoda, S.; Kitagawa, S. Nanoporous Nanorods Fabricated by Coordination Modulation and Oriented Attachment Growth. *Angew. Chem. Int. Ed.* **2009**, *48*, 4739–4743.
44. Cravillon, J.; Nayuk, R.; Springer, S.; Feldhoff, A.; Huber, K.; Wiebcke, M. Controlling zeolitic imidazolate framework nano- and microcrystal formation: Insight into crystal growth by time-resolved *in situ* static light scattering. *Chem. Mater.* **2011**, *23*, 2130–2141.
45. Pan, Y.; Liu, Y.; Zeng, G.; Zhao, L.; Lai, Z. Rapid synthesis of zeolitic imidazolate framework-8 (ZIF-8) nanocrystals in an aqueous system. *Chem. Commun.* **2011**, *47*, 2071–2073.
46. Goellner, V.; Armel, V.; Zitolo, A.; Fonda, E.; Jaouen, F. Degradation by Hydrogen Peroxide of Metal-Nitrogen-Carbon Catalysts for Oxygen Reduction. *J. Electrochem. Soc.* **2015**, *162*, H403–H414.
47. Yuan, S.; Shui, J.-L.; Grabstanowicz, L.; Chen, C.; Commet, S. Reprogle, B.; Xu, T.; Yu, L.; Liu, D.-J. A Highly Active and Support-Free Oxygen Reduction Catalyst Prepared from Ultrahigh-Surface-Area Porous Polyporphyrin. *Angew. Chem. Int. Ed.* **2013**, *52*, 1–6.